

Beating stellar systematic error floors using transit-based densities

JASON D. EASTMAN,¹ HANNAH DIAMOND-LOWE,² AND JAMIE TAYAR³

¹*Center for Astrophysics | Harvard & Smithsonian, 60 Garden St, Cambridge, MA 02138, USA*

²*National Space Institute, Technical University of Denmark, Elektrovej 328, 2800 Kgs. Lyngby, Denmark*

³*Department of Astronomy, University of Florida, Bryant Space Science Center, Stadium Road, Gainesville, FL 32611, USA*

ABSTRACT

It has long been understood that the light curve of a transiting planet constrains the density of its host star. That fact is routinely used to improve measurements of the stellar surface gravity, and has been argued to be an independent check on the stellar mass. Here we show how the stellar density can also provide meaningful constraints on the radius and effective temperature of the star. This additional constraint is especially significant when we properly account for the 4.2% radius and 2.4% temperature systematic errors inherent in the stellar evolutionary and atmospheric models. In the typical case, we can measure stellar radii to 3% and temperatures to 1.75%. In the best real-world cases, we can infer radii to 1.7% and temperatures to 1.2% – well below the systematic floors from stellar models alone – which can improve the precision in the planetary parameters by a factor of two. We explain in detail the mechanism that makes it possible and show a demonstration of the technique for a near-ideal system, WASP-4.

We also show that both the statistical and systematic uncertainties in the parallax from *Gaia* DR3 are often a significant component of the uncertainty in L_* and must be treated carefully. Taking advantage of our technique requires simultaneous models of the stellar evolution, bolometric flux (e.g., a stellar spectral energy distribution), and the planetary transit, while accounting for the systematic errors in each, as is done in EXOFASTv2.

Keywords: planetary systems, planets and satellites: detection, stars

1. INTRODUCTION

Any measurement of the mass, radius, or temperature of an exoplanet depends directly on those same quantities for its host star. As a result, the exploding interest in exoplanets has re-kindled a broad interest in measuring precise and accurate stellar parameters in order to derive precise and accurate planetary parameters. This has correctly given rise to the oft-repeated phrase “know thy star, know thy planet.”

Precise parallax measurements and all-sky, precise optical photometry by *Gaia* (Gaia Collaboration et al. 2016, 2018), coupled with all-sky infrared photometry from 2MASS (Skrutskie et al. 2006) and WISE (Wright et al. 2010) have enabled a new era of precision stellar astrophysics. Now, for nearly all exoplanet host stars, the uncertainties in stellar parameters are no longer limited by the measurements, but by the stellar evolutionary and atmospheric models, requiring an understanding of the underlying systematic errors in those models. We need great care not to be overly confident in our

results, but we must also not be overly conservative, lest we fail to recognize the significance of a precise detection.

Tayar et al. (2022) published a guide for reasonable systematic error floors by carefully enumerating the sources of systematic error, tracing fundamental calibrations back to their origins, and determining the discrepancies between different groups with different instruments and different models. They find systematic errors that are larger than uncertainties often quoted in the exoplanet community.

However, Tayar et al. (2022) does not consider the impact of an additional constraint for transiting exoplanet hosts that is nearly free of systematic error: the stellar density from the transit light curve. The ability for the transit light curve to measure the stellar density, ρ_* , was first recognized by Seager & Mallén-Ornelas (2003) for planets in circular orbits. Planets in eccentric orbits complicate the computation and generally add additional uncertainty, but with a known eccentricity and argument of periastron (typically from RVs, but also potentially through primary and secondary transits or, in the future, astrometry), we can still derive the stellar density from a transit light curve (see e.g., Eastman et al. 2019).

By definition, we need only two of the stellar mass (M_*), radius (R_*), density (ρ_*), or surface gravity ($\log g_*$) to derive the others, as these are mathematically and exactly related to one another. Then, we only need either the bolometric flux (F_{bol}) or stellar temperature (T_{eff}) – and a precise distance from *Gaia* – to determine the other, again, by definition.

This concept is not new. [Beatty et al. \(2017\)](#) argued, and [Stevens et al. \(2018\)](#) later expanded on the idea that, with an R_* from SED fitting and ρ_* from transits, we can derive an M_* free from the systematic errors of stellar evolutionary models. Unfortunately, [Stevens et al. \(2018\)](#) showed – and we will confirm – that even an optimistic statistical uncertainty in the stellar mass we can obtain this way is well above what is thought to be a realistic systematic uncertainty in M_* from stellar models. In addition, they still must rely on systematics-dominated determinations of F_{bol} to infer the stellar radius in the first place.

Here, we show an idea similar to [Stevens et al. \(2018\)](#), but instead of using ρ_* and deriving M_* with a known R_* , we derive R_* with a known M_* . Then, with a measured L_* , we derive T_{eff} . Assuming the systematic error floors from [Tayar et al. \(2022\)](#) on M_* and L_* , and the transit-derived measurement of ρ_* , we simply propagate those floors to significantly more precise inferred values of R_* and T_{eff} than the measurement floors found by [Tayar et al. \(2022\)](#) using models alone. We go through the math in §2, and discuss systematic errors in §3. We talk about best practices in §4. Finally, we look at a best-case scenario in refitting WASP-4b in §5, and we discuss the implications of this work in §6.

2. MATHEMATICAL VALIDATION

2.1. M_* from R_*

First, we re-derive results similar to [Stevens et al. \(2018\)](#), by starting with the definition of the stellar density,

$$\rho_* \equiv \frac{3M_*}{4\pi R_*^3}. \quad (1)$$

Assuming Gaussian and uncorrelated errors, we can use standard error propagation techniques to show the uncertainty in M_* , σ_{M_*} , is given by

$$\sigma_{M_*}^2 = \left(\frac{\partial M_*}{\partial \rho_*} \right)^2 \sigma_{\rho_*}^2 + \left(\frac{\partial M_*}{\partial R_*} \right)^2 \sigma_{R_*}^2 \quad (2)$$

where σ_{ρ_*} is the uncertainty in the stellar density measured from transits, and σ_{R_*} is the uncertainty in the stellar radius derived from F_{bol} . After evaluating the derivatives, we can simplify equation 2 by dividing both sides by M_*^2 to express it as a fractional uncertainty.

$$\left(\frac{\sigma_{M_*}}{M_*} \right)^2 = \left(\frac{\sigma_{\rho_*}}{\rho_*} \right)^2 + \left(\frac{3\sigma_{R_*}}{R_*} \right)^2 \quad (3)$$

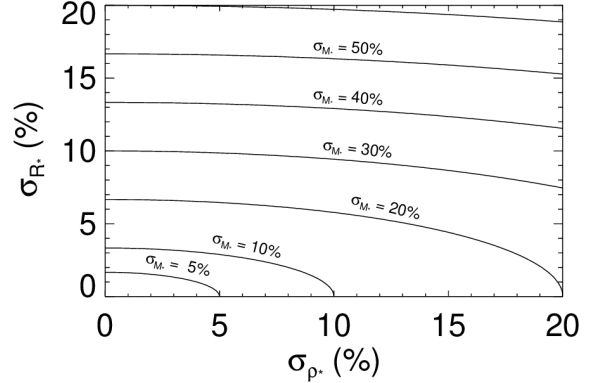


Figure 1. A contour plot of the percent error in M_* as a function of the percent errors in ρ_* and R_* , derived from equation 3. We see that the dependence on σ_{R_*} is strong, and with a typical σ_{ρ_*} of 10%, the resulting constraint on M_* is not particularly informative. Even with no error in ρ_* , the systematic floor in R_* of $\sim 4.2\%$ implies an error of 13% in stellar mass, which is not competitive with evolutionary models.

Table 1. Summary of relevant parameters from simulated fits by [Stevens et al. \(2018\)](#)

	e=b=0	%	e=0.5, b=0	%	e=0, b=0.75	%
M_*	$1.146^{+0.075}_{-0.092}$	7.3%	$1.20^{+0.21}_{-0.23}$	18.3%	$1.18^{+0.23}_{-0.19}$	17.8%
R_*	$1.046^{+0.017}_{-0.016}$	1.6%	$1.043^{+0.017}_{-0.018}$	1.6%	$1.047^{+0.018}_{-0.017}$	1.7%
ρ_*	$1.424^{+0.049}_{-0.097}$	5.1%	$1.49^{+0.23}_{-0.28}$	17.1%	$1.46^{+0.26}_{-0.21}$	16.1%
T_{eff}	5710^{+160}_{-140}	2.6%	5740^{+160}_{-150}	2.7%	5700^{+170}_{-140}	2.7%

NOTE—Percent errors were calculated by averaging upper and lower errors.

In Figure 1, we show a contour plot of the percent error in M_* as function of the percent errors in ρ_* and R_* , using equation 3. We see the percent error in R_* is multiplied by a factor of three when it propagates to the error in M_* , which makes it difficult to get a small σ_{M_*} .

[Stevens et al. \(2018\)](#) does three simulated fits, one with e=0 (fixed), b=0; one with e=0.5, b=0; and one with e=0 (fixed), b=0.75 to show the dependence on the measured precision of ρ_* on the eccentricity and impact parameter. The percent errors from their simulations on R_* , M_* , ρ_* , and T_{eff} are summarized in Table 1.

While their quoted uncertainty in R_* ignores sources of systematic error, we can still use these results to confirm our expectations given Figure 1 and equation 3. Indeed, in the first case, with 5.1% errors on ρ_* and 1.6% errors on R_* , Equation 2 predicts a 7.0% uncertainty in M_* , completely consistent with the measured value of 7.3%. In the second

case, with 17.1% errors on ρ_* and 1.6% errors on R_* , equation 2 predicts an 17.8% uncertainty in M_* , completely consistent with the measured value of 18.3%. And finally, in the last case, with 16.1% errors on ρ_* and 1.7% errors on R_* , we predict a 17.0% uncertainty in M_* , again consistent with the measured value of 17.8%.

The uncertainty, even in the best case they present and ignoring systematic errors in F_{bol} when they derive R_* , is well above the systematic uncertainties presumed in most stellar models because the stellar radius uncertainty is compounded, leading to a much larger percent error in the stellar mass.

For certain ideal systems (tidally circularized, deep, well measured, like WASP-4b), the error on ρ_* can be $\sim 1\%$. Even so, coupled with the 4.2% systematics-dominated uncertainty in R_* recommended by [Tayar et al. \(2022\)](#), the resultant mass uncertainty is still $\sim 13\%$. We also note that the uncertainty in T_{eff} from [Stevens et al. \(2018\)](#) is relatively large because they have avoided using an evolutionary model, and so the SED is working to constrain both R_* and T_{eff} .

So, while their method may serve as a rough, independent check on systematics, it is unlikely to be helpful in a significant number of cases.

2.2. R_* from M_*

Instead, we can infer R_* from M_* and ρ_* . Again, starting from equation 1, we instead propagate the uncertainties in M_* to R_* .

$$\sigma_{R_*}^2 = \left(\frac{\partial R_*}{\partial \rho_*}\right)^2 \sigma_{\rho_*}^2 + \left(\frac{\partial R_*}{\partial M_*}\right)^2 \sigma_{M_*}^2 \quad (4)$$

As before, we evaluate and simplify by dividing both sides by R_*^2 to express it as a percent uncertainty.

$$\left(\frac{\sigma_{R_*}}{R_*}\right)^2 = \left(\frac{\sigma_{\rho_*}}{3\rho_*}\right)^2 + \left(\frac{\sigma_{M_*}}{3M_*}\right)^2 \quad (5)$$

Here, we see that, instead of magnifying the errors as when we determined M_* , our input fractional errors are reduced by a factor of 3. Thus, the resultant percent uncertainty in R_* can be much lower than the input percent uncertainties in M_* and ρ_* .

Figure 2 shows the same contour plot, but now with the inferred percent error in R_* as a function of percent errors in ρ_* and M_* (equation 5). Of course, getting M_* usually requires stellar evolutionary models, but even assuming a systematic floor of 5% on M_* from stellar models, if we measure ρ_* to 1%, we get 1.7% errors on R_* —almost three times better than the recommended systematic floor in the stellar models. And while our determination of the stellar radius hinges on the systematics-dominated stellar evolution models, these errors are already included in the computation as σ_{M_*} . For everything else, we rely on well established physics (i.e., Kepler’s law) and definitions (e.g., equation 1).

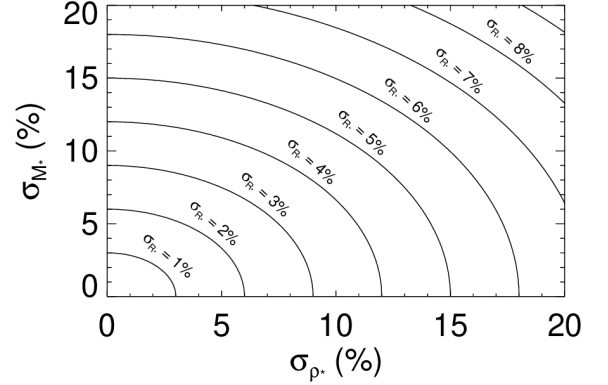


Figure 2. A contour plot of the percent error in R_* as a function of the percent errors in ρ_* and M_* , derived in equation 5. We see that the dependence on M_* is much weaker, and with a typical σ_{ρ_*} of 10%, the resulting constraint on R_* can be well below the systematic floor from evolutionary models. In the best cases, we can measure ρ_* to $\sim 1\%$, resulting in R_* uncertainties of $\sim 1.7\%$ —almost entirely dominated by the systematic floor in M_* .

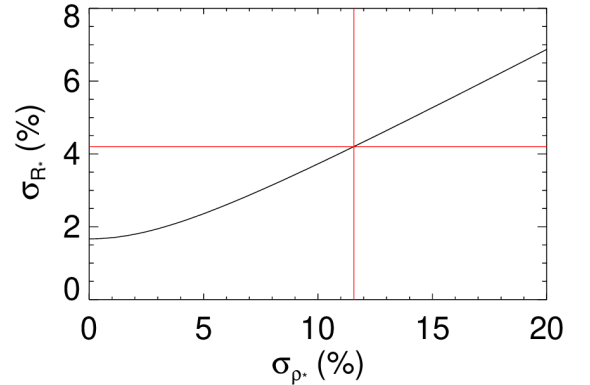


Figure 3. A plot of σ_{R_*} as a function of σ_{ρ_*} , assuming $\sigma_{M_*} = 5\%$. The break-even point, where $\sigma_{R_*} = 4.2\%$ from [Tayar et al. \(2022\)](#), is shown as a vertical red line and corresponds to $\sigma_{\rho_*} \sim 11.5\%$.

Assuming our M_* error is 5%, we can plot σ_{R_*} as a function of σ_{ρ_*} , as shown in Figure 3, where the break-even point is shown as a vertical red line at $\sim 11.5\%$. That is, measuring ρ_* to better than 11.5%—which is typical—allows us to measure the stellar radius to better than the systematic errors inherent in stellar models.

2.3. T_{eff} from L_*

Now we can propagate the error in R_* along with a reasonable floor in L_* to T_{eff} with the definition of the stellar luminosity,

$$L_* \equiv 4\pi R_*^2 \sigma_{SB} T_{\text{eff}}^4, \quad (6)$$

where σ_{SB} is the Stefan-Boltzmann constant. Following a similar procedure as above, we write

$$\sigma_{T_{\text{eff}}}^2 = \left(\frac{\partial T_{\text{eff}}}{\partial L_*} \right)^2 \sigma_{L_*}^2 + \left(\frac{\partial T_{\text{eff}}}{\partial R_*} \right)^2 \sigma_{R_*}^2. \quad (7)$$

Again, we evaluate and simplify by dividing by T_{eff}^2 to express it in terms of fractional errors.

$$\left(\frac{\sigma_{T_{\text{eff}}}}{T_{\text{eff}}} \right)^2 = \left(\frac{\sigma_{L_*}}{4L_*} \right)^2 + \left(\frac{\sigma_{R_*}}{2R_*} \right)^2 \quad (8)$$

We see the fractional uncertainty in L_* is cut by a factor of 4 as it propagates to T_{eff} , so the uncertainty in R_* quickly dominates. Even so, the uncertainty in R_* is also halved, leading to surprisingly precise determinations of T_{eff} .

Figure 4 shows a contour plot of equation 8 and we see that, for the recommended systematic error floor of 2% on L_* from [Tayar et al. \(2022\)](#) and our best-case error on R_* of 1.7% above, we get 0.9% errors on T_{eff} . That is 50 K for a solar type star – far better than the typically assumed systematic error floors on T_{eff} , which are derived from the complexities of calibrations and gaps in our knowledge of stellar evolution. Instead, these are very simply derived from an independent constraint on ρ_* (based on Kepler’s law) and error propagation, with well-motivated systematic error floors on L_* and M_* from [Tayar et al. \(2022\)](#).

If we assume that $\sigma_{M_*} = 5\%$, we compute the same σ_{R_*} as in §2.2. Then we assume $\sigma_{L_*} = 2\%$, and plug those into equation 8 to plot $\sigma_{T_{\text{eff}}}$ as a function of σ_{ρ_*} , in Figure 5. The break-even point is shown as a vertical red line at $\sigma_{\rho_*} \sim 13\%$. That is, measuring the precision in ρ_* to better than 13% can improve the precision of the T_{eff} to better than the 2.4% error floor from [Tayar et al. \(2022\)](#).

We note that large systematic errors in L_* – far exceeding the 2% suggested by [Tayar et al. \(2022\)](#) – are possible if we fail to identify visual or bound companions that are blended in the broadband photometry. This would introduce large systematic errors in the SED model, increasing the inferred stellar radius and/or temperature. However, these biases are subject to the same sort of scaling – a bias of 5% in T_{eff} would require an undetected companion with 20% of the flux of the primary, which would likely be detected in high resolution spectroscopy.

2.3.1. Bolometric flux, distance systematics

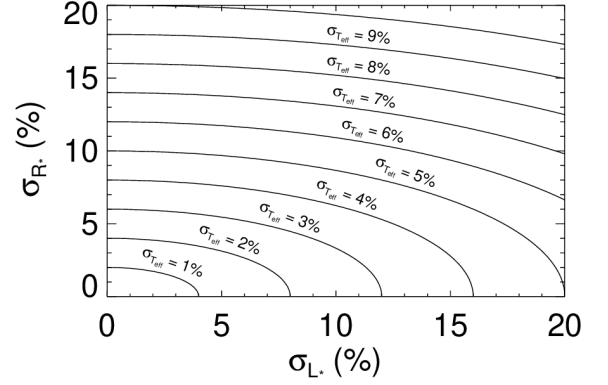


Figure 4. A contour plot of the percent error in T_{eff} as a function of the percent errors in R_* and F_{bol} , derived equation equation 7. We see that the dependence on M_* is much weaker, and with a typical σ_{R_*} of 3% and a systematic floor of $F_{\text{bol}} \sim 2\%$, the resulting constraint on T_{eff} can be $\sim 1.5\%$ – well below the systematic floor from evolutionary models, SED models, or spectra. In the best cases, we can measure R_* to $\sim 1.7\%$ and T_{eff} uncertainties of just under 1%.

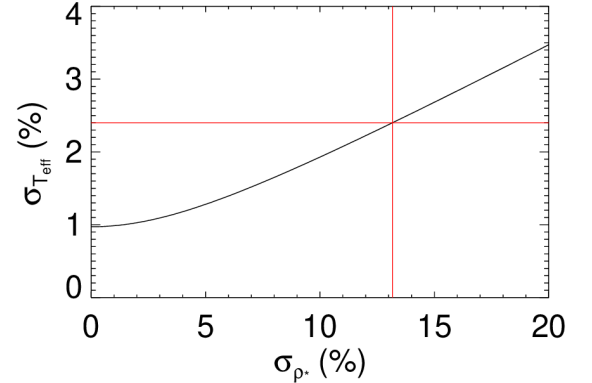


Figure 5. A plot of $\sigma_{T_{\text{eff}}}$ as a function of σ_{ρ_*} , assuming $\sigma_{M_*} = 5\%$. The break-even point, where $\sigma_{T_{\text{eff}}} = 2.4\%$ from [Tayar et al. \(2022\)](#), is shown as a vertical red line and corresponds to $\sigma_{\rho_*} \sim 13\%$.

We can also write the T_{eff} uncertainty in terms of the bolometric flux, which is the observed quantity,

$$F_{\text{bol}} \equiv \sigma_{SB} T_{\text{eff}}^4 \left(\frac{R_*}{d} \right)^2, \quad (9)$$

where d is the distance to the star. Following our usual procedure, the fractional uncertainty in T_{eff} becomes

$$\left(\frac{\sigma_{T_{\text{eff}}}}{T_{\text{eff}}} \right)^2 = \left(\frac{\sigma_d}{2d} \right)^2 + \left(\frac{\sigma_{F_{\text{bol}}}}{4F_{\text{bol}}} \right)^2 + \left(\frac{\sigma_{R_*}}{2R_*} \right)^2 \quad (10)$$

When the uncertainty in the distance (e.g., from *Gaia*) is negligible, equations 8 and 10 are functionally identical. [Tayar et al. \(2022\)](#) state that the vast majority of planet hosting stars have negligible distance uncertainties, and they ignore the distance term, not distinguishing between systematics in F_{bol} and systematics in L_* .

Indeed, 75% of planet hosting stars have fractional distance uncertainties less than the 4.2% systematic stellar radius floor they found, and so the uncertainty in radius usually dominates the error budget in L_* without an external constraint on ρ_* from transits. However, only 40% of planet hosts have distance uncertainties below 1.7% – the smallest systematic uncertainty in the radius we might expect using our method. Therefore, the uncertainty in the parallax – and its systematic uncertainty – is an important consideration in general.

We clarify that the systematic floor quoted on L_* from [Tayar et al. \(2022\)](#) is entirely based on the systematic errors inherent in F_{bol} , leaving an important additional source of systematic error in the luminosity from the distance.

There has been a wide recognition that *Gaia* DR2 has systematic errors in the measured parallax, with estimates ranging from 30 - 80 μs that likely depend on magnitude, color, and ecliptic latitude ([Stassun & Torres 2018](#); [Lindgren et al. 2018](#); [Zinn et al. 2019](#)). *Gaia* EDR3/DR3 is better, but still has systematics estimated at the “few tens of μs ” ([Lindgren et al. 2021](#)).

Because d is determined from the parallax, ϖ

$$d \equiv \frac{1''}{\varpi} \text{ pc}, \quad (11)$$

we can propagate the uncertainty in ϖ , σ_{ϖ} , to the fractional uncertainty in distance, σ_d/d , as

$$\frac{\sigma_d}{d} = \frac{\sigma_{\varpi}}{\varpi}. \quad (12)$$

We plot Equation 12 as a function of distance in Figure 6, assuming a systematic floor of 30 μs from *Gaia* DR3. This systematic floor is the dominant source in the L_* computation for stars beyond 1400 pc when we assume the $\sigma_{R_*} = 4.2\%$ from [Tayar et al. \(2022\)](#), corresponding to 8% of planet hosts. When we use our systematic floor of 1.7% using a precise ρ_* , the distance systematic is the dominant source of error in L_* when stars are beyond 567 pc, corresponding to 42% of planet hosts.

So these systematics cannot, in general, be ignored. Since *Gaia* DR3 has significantly reduced systematic errors, its use is highly recommended over *Gaia* DR2. DR4 is expected to further reduce systematic uncertainties. It is also important to correct for these systematics as best as possible. We note the EXOFASTv2 includes MKTICSED, which applies the EDR3/DR3 correction to the parallax described in [Linde-](#)

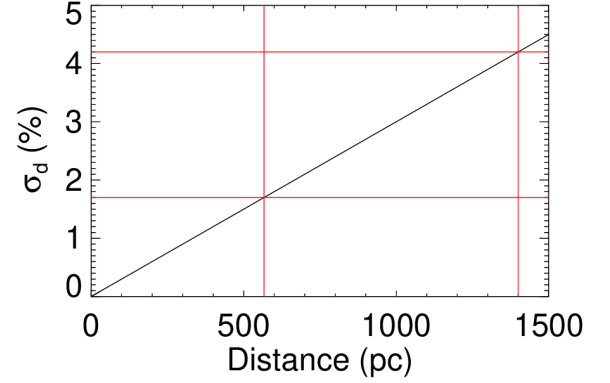


Figure 6. A plot of the level of systematic error in *Gaia* as a function of distance. The black line shows a 30 μs systematic uncertainty in *Gaia* DR3 estimated by [Lindgren et al. \(2021\)](#), which dominates the luminosity systematics at ~ 600 pc and ~ 1400 pc when the R_* uncertainties are at the systematic limits of 1.7% and 4.2%, marked as red lines.

[gren et al. \(2021\)](#), which parameterizes the systematic error as a function of color, magnitude, and ecliptic latitude.

2.4. $\log g_*$ from ρ_* and R_*

Measuring $\log g_*$ from spectra is both imprecise and inaccurate, with systematic error floors of ~ 0.1 dex ([Torres et al. 2012](#)).

However, using the same procedure as above, we can propagate errors on ρ_* and R_* to $\log g_*$ and achieve more than an order of magnitude better precision. The fact that the transit can constrain $\log g_*$ has long been appreciated (e.g. [Winn et al. 2008](#)), but it has never been stated in this kind of formalism.

So we start with the definition of the stellar surface gravity,

$$\log g_* \equiv \log_{10} \left(\frac{GM_*}{R_*^2} \right), \quad (13)$$

except we refactor to put it in terms of the directly-measured ρ_* instead of the systematics-dominated M_* .

$$\log g_* = \log_{10} \left(\frac{4\pi G}{3} \rho_* R_* \right), \quad (14)$$

we propagate errors as before,

$$\sigma_{\log g_*}^2 = \left(\frac{\partial \log g_*}{\partial \rho_*} \right)^2 \sigma_{\rho_*}^2 + \left(\frac{\partial \log g_*}{\partial R_*} \right)^2 \sigma_{R_*}^2 \quad (15)$$

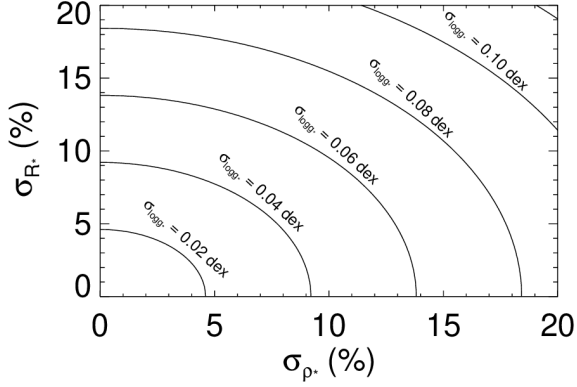


Figure 7. A contour plot of the error in $\log g_*$ as a function of the percent errors in ρ_* and R_* , derived from equation 18. A typical spectroscopic constraint is 0.1 dex. For precise values of ρ_* , we can do more than an order of magnitude better.

Here the logs already express the $\log g_*$ error in terms of the fractional errors in ρ_* and R_* , so we just evaluate the derivatives and simplify.

$$\sigma_{\log g_*}^2 = \left(\frac{\sigma_{\rho_*}}{\ln(10)\rho_*} \right)^2 + \left(\frac{\sigma_{R_*}}{\ln(10)R_*} \right)^2 \quad (16)$$

We show the contour plot of equation 16 in Figure 7, noting that the error in $\log g_*$ is in dex, not percent as for previous, similar plots. A typical spectroscopic constraint on $\log g_*$ is 0.1 dex, which is more than an order of magnitude worse for the best cases where $\sigma_{\rho_*} \sim 1\%$ and $\sigma_{R_*} \sim 1.7\%$ where we get an uncertainty of ~ 0.008 dex.

2.5. $\log g_*$ from M_* and R_*

In addition, even propagating sensible systematic error floors in M_* and R_* from evolutionary and SED models, we can typically determine a $\log g_*$ that is still more than twice as precise as spectra. That is, in the post-*Gaia* era, we should only rely on a spectroscopic determination of $\log g_*$ in the rare cases where *Gaia* has not measured the distance of a planet host or when the SED cannot be trusted (e.g., due to a blend).

To show this, we repeat the exercise starting from equation 13, and again propagate errors,

$$\sigma_{\log g_*}^2 = \left(\frac{\partial \log g_*}{\partial M_*} \right)^2 \sigma_{M_*}^2 + \left(\frac{\partial \log g_*}{\partial R_*} \right)^2 \sigma_{R_*}^2 \quad (17)$$

which evaluates to

$$\sigma_{\log g_*}^2 = \left(\frac{\sigma_{M_*}}{\ln(10)M_*} \right)^2 + \left(\frac{2\sigma_{R_*}}{\ln(10)R_*} \right)^2 \quad (18)$$

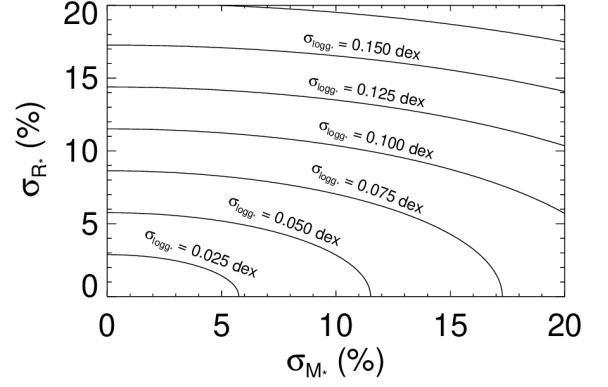


Figure 8. A contour plot of the percent error in $\log g_*$ as a function of the percent errors in M_* and R_* , derived from equation 17. A typical spectroscopic constraint of 0.1 dex corresponds to 2% error for a solar type star. When we get systematic error dominated values for M_* and R_* (without a transit-density), we still do about 2x better than spectroscopy.

And we show the contour plot of equation 18 in Figure 8. We can see that for the typical exoplanet host star, which is systematics-dominated ($\sigma_{M_*} \sim 5\%$ and $\sigma_{R_*} \sim 4.2\%$), we get a $\log g_*$ precision of ~ 0.042 dex – more than a factor of two better than spectroscopy.

If we assume that our $\sigma_{M_*} = 5\%$, we compute the same σ_{R_*} as in §2.2. Then we plug those into equation 16 to plot $\sigma_{\log g_*}$ as a function of σ_{ρ_*} , in Figure 9. The break-even point is shown as a vertical red line at $\sigma_{\rho_*} \sim 9\%$. That is, measuring ρ_* to better than 9% can improve the precision of the $\log g_*$ to better than the 0.042 dex derived from the floors in Tayar et al. (2022).

3. SYSTEMATIC ERRORS IN ρ_*

The derivation of ρ_* from transits is straight-forward and has been done in many places (e.g. Winn 2010). For context, we repeat it here. Starting with Kepler’s law and the known planetary period, P,

$$P^2 = \frac{4\pi^2 a^3}{G(M_* + M_P)}, \quad (19)$$

we refactor in terms of ρ_* and solve,

$$\rho_* = \frac{3\pi}{GP^2} \left(\frac{a}{R_*} \right)^3 \frac{M_*}{M_* + M_P}. \quad (20)$$

If we wish, we can refactor equation 20 in terms of R_P and ρ_P , which makes the negligible planetary term more obvious.

$$\rho_* = \frac{3\pi}{GP^2} \left(\frac{a}{R_*} \right)^3 - \left(\frac{R_P}{R_*} \right)^3 \rho_P. \quad (21)$$

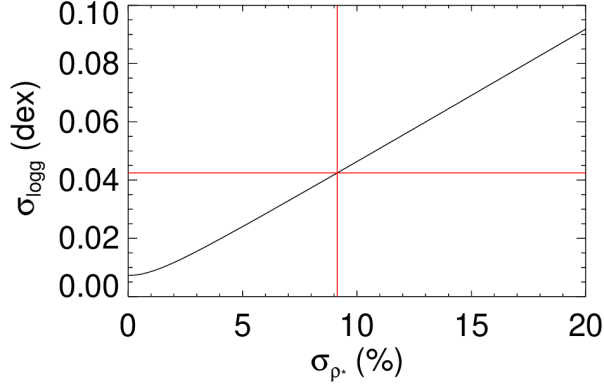


Figure 9. A plot of $\sigma_{\log g_*}$ as a function of σ_{ρ_*} , assuming $\sigma_{M_*} = 5\%$. The break-even point of $\log g_* = 0.042$ dex, where $\sigma_{M_*} = 5\%$ and from [Tayar et al. \(2022\)](#), is shown as a vertical red line and corresponds to $\sigma_{\rho_*} \sim 9\%$.

Figure 3 shows the 5% systematic error in M_* dominates as long as $\sigma_{\rho_*} \lesssim 2\%$, so here we aim to convince the reader that the sources of systematic error in ρ_* are well below that floor, and so no matter what statistical precision we achieve in ρ_* , we can trust the derived uncertainties in R_* and T_{eff} .

If the companion mass is less than $20 M_J$ for a solar type star, ignoring the planetary mass entirely contributes less than 2% to the ρ_* , so we drop that term moving forward, and the fractional uncertainty in ρ_* becomes

$$\left(\frac{\sigma_{\rho_*}}{\rho_*}\right)^2 = \left(\frac{\sigma_P}{P}\right)^2 + \left(\frac{3\sigma_{a/R_*}}{a/R_*}\right)^2. \quad (22)$$

3.1. a/R_*

For the majority of systems, the most problematic component in computing ρ_* is a/R_* . Not only is the measurement less straight-forward, but its percent uncertainty is magnified by three when propagating to ρ_* , as we see in equation 22.

3.1.1. Eccentricity

First, a/R_* is not the observable, the transit duration is. For non-grazing, circular orbits, the transit duration translates to a direct constraint on a/R_* , but for eccentric orbits, the observable is better approximated by

$$\frac{a}{R_*} \frac{\sqrt{1-e^2}}{1+e\sin\omega_*}. \quad (23)$$

That means we must also know or assume the planetary eccentricity and argument of periastron. [Stevens et al.](#) (Equation 79 and Figure 10, 2018) shows that, for an eccentricity known to better than $\sim 1.5\%$ – and more lax for smaller eccentricities – the uncertainty in e contributes negligibly to the uncertainty in ρ_* .

Planets in very short periods can be assumed to be tidally circularized ([Adams & Laughlin 2006](#)). Given the small impact at low eccentricities, even if the planet is not strictly circularized, the error introduced to ρ_* is indeed negligible.

For other systems, we must rely on radial velocities, and we inherit the systematic errors of the spectrograph. The impact on the inferred eccentricity depends heavily on the spectrograph and the planet. In many cases, particularly for Hot Jupiters most amenable to measuring ρ_* , the statistical error dominates the systematic error, but for systems where the RV semi-amplitude is comparable to the instrumental precision, the eccentricity uncertainty is likely dominant.

Or, we can rely on the combination of the timing and duration of both the primary and secondary transit, inheriting the systematic errors of the photometric instrument and the clock. This typically yields extremely precise measurements of eccentricity, well below 1.5%.

In the future, we may be able to use *Gaia* DR4 to determine the eccentricity for a handful of (nearby, long period) transiting systems, inheriting the systematic errors on its astrometry.

Ultimately, we need to be mindful of systematic error sources when the eccentricity uncertainty exceeds $\sim 1.5\%$ – which is often, and may ultimately limit the number of stars where we can do such measurements. A campaign to measure precise eccentricities through secondary eclipse timing may dramatically broaden the number of stars where this technique is practical.

3.1.2. Grazing transits

When the transit is grazing, significant degeneracies are introduced between the duration (i.e., a/R_*), inclination, and planetary radius. Because of that degeneracy, it is unlikely that grazing transits will provide a sufficient constraint on a/R_* .

3.1.3. Limb darkening

An a priori constraint on the limb darkening is often derived from stellar atmospheric models. Theoretical limb darkening coefficients can differ dramatically from empirical measurements, especially for non-solar ($T_{\text{eff}} \lesssim 5000$ K or $T_{\text{eff}} \gtrsim 7000$ K) stars ([Patel & Espinoza 2022](#)). In addition, the common choice of a quadratic limb darkening law is not, in detail, correct. As both a/R_* and the limb darkening depend on the shape of the transit, errors in the limb darkening may bias the inferred values of a/R_* .

With sufficiently precise light curves, we can measure the limb darkening directly and remove the reliance on the stellar atmospheric models. Even in simulated cases where the theoretical limb darkening differs from the actual limb darkening by 0.1 in each quadratic term (nominally twice the assumed model uncertainty), its impact on the stellar parameters is negligible. Still, we recommend that when the light

curve is sufficiently precise to directly measure the limb darkening, the a priori constraint from the tables should be disabled. When using EXOFASTv2, if the reported precision of the limb darkening parameters is smaller than the 0.05 systematic error assumed in the tables, the tables should not be used.

In addition, the choice of the limb darkening law can still bias the fit. EXOFASTv2 only implements the quadratic limb darkening law, introducing a systematic error floor. However, Mandel & Agol (2002) showed the error introduced here is typically below the noise floor, and thus negligible as it propagates to ρ_* .

3.1.4. Non-Keplerian Motion

The foundation of our derivation of ρ_* is Kepler’s law, but the presence of additional bodies and tidal forces mean that nothing follows Kepler’s law to infinite precision. For a system with TTVs, a/R_* changes over time, but surely that has no impact on the stellar density. EXOFASTv2 assumes Keplerian orbits, but computational time is the only reason we hesitate to implement an N-body code to compute the planetary orbits. Given that the transit duration and stellar density is never explicitly defined in the transit model, it is likely that an accurate computation of any non-Keplerian motion would provide a similar constraint on the stellar density, but a detailed investigation of this is beyond the scope of this paper.

3.2. Period

The planetary period is directly measured from the frequency of transits, leveraged with long baselines between transits, often resulting in part per billion precision in the planetary period. However, it is worth noting that we universally introduce a systematic error in the observed period that is statistically significant in many systems today. Because stars are moving with respect to the Solar System Barycenter frame, there is a light travel time effect that changes the observed frequency of transits by the systemic velocity, γ , divided by the speed of light, c

$$\Delta P = \gamma/c. \quad (24)$$

But the reported planetary period is universally given in the Solar System Barycenter frame. Given a typical systemic velocity of $\sim 10 \text{ km s}^{-1}$, this $\sim 30 \text{ ppm}$ effect amounts to about 30 seconds in a 10 day period, which is easily measurable today for the vast majority of transiting systems. Even EXOFASTv2, which does transform the observed times to the target frame before computing the model, ignores this effect because the radial velocity is often measured from a reference spectrum taken at an earlier time, and so the absolute systemic velocity is often unknown. In addition, reporting the true period in the target’s barycentric frame would lead to

confusion in propagating the ephemerides that are practically important.

However, the impact of this error on ρ_* (or any observable we care about) is dwarfed by other errors. The 30 ppm effect is 5000 times lower than our threshold, so we safely ignore it.

4. IMPLEMENTATION

Despite the simplicity of the argument, in many cases, a fundamentally new approach must be developed to take advantage of it. We can no longer simply interpolate an evolutionary grid to find the stellar parameters, as is commonly done. Nor can we simply separate the stellar and planetary model, as is also often done. The additional stellar density constraint over-constrains the evolutionary model grids, requiring optimization of competing constraints while simultaneously respecting the systematic error floors inherent in the evolutionary and atmospheric models. In addition, the constraints are often correlated in important ways, and those covariances must be known and applied with care if iterating between the stellar and planetary models to improve the precision of both. It is not enough to apply Gaussian, uncorrelated priors with each iteration.

As far as we are aware, EXOFASTv2 is unique in this regard – among private and public exoplanet modeling codes. The link between the stellar density and the transit photometry has been at the heart of EXOFAST since its inception (Eastman et al. 2013), and the link between T_{eff} , R_* , and L_* have been coded within EXOFASTv2 since SED fitting was added in January 2017 (Eastman et al. 2019). Despite only deeply understanding the mechanism now, EXOFASTv2 has long respected these relations and has been capable of using the transit-derived density to determine stellar parameters that are less dependent on the systematic floors of evolutionary models.

However, until *Gaia* DR2 in April 2018, we could not always measure sufficiently precise luminosities, and up until October 2020, we ignored systematic errors in the SED model, which resulted in many fits with underestimated uncertainties. In July 2022, another update now allows users to specify their own systematic error floors on the stellar evolutionary models so that they may more accurately reflect those found by Tayar et al. (2022) rather than use the default ad hoc systematic error floors as a function of stellar mass described in Eastman et al. (2019) and summarized in equation 25:

$$\sigma = 0.03 - 0.025 \log M_* + 0.045 (\log M_*)^2. \quad (25)$$

We warn the user that the sample used by Tayar et al. (2022) were near solar type stars, and for such stars, Tayar et al. (2022) showed the default $\sim 3\%$ errors are EXOFASTv2 uses are likely slight underestimates of the systematic floors. However, for lower mass stars, the systematic errors are

likely much larger than the sample [Tayar et al. \(2022\)](#) explored, and our default ad hoc value of $\sim 10\%$ is likely more appropriate.

Finally, while the true nature of systematic errors is still poorly understood, we presume that all theoretical models share similar systematics, and so any combination of stellar theoretical models should not drive the uncertainties below the floors described in [Tayar et al. \(2022\)](#). When using multiple theoretical models (e.g., MIST and SED) with separate floors on the same parameters, the floors should be further inflated by the square root of the number of models so that the combined model systematics are still below the desired floors. Checking that the floors are as desired with a star-only fit is a good standard practice.

5. WASP-4b

An MCMC code does not assume the errors are Gaussian or uncorrelated, and so we can check that our derivation’s assumptions are reasonable by fitting a real-world system with a variety of constraints to check for such correlations and to see if they recreate our uncorrelated expectations.

WASP-4b is a planet in a short period (1.34 days) which we can reasonably assume is tidally circularized and so we know the eccentricity exactly, improving the precision in ρ_* (see §3.1.1). In addition, it has been observed in 3 TESS sectors at 2 minute cadence, with a very long baseline between the TESS observations and the 8 discovery light curves in 2007 ([Wilson et al. 2008](#); [Gillon et al. 2009](#); [Winn et al. 2009](#)). Many of those discovery light curves were observed in Sloan z’ band and the transit is nearly edge on, which minimizes the covariance between density, impact parameter, and limb darkening. Finally, the transit is very deep (2.4%). All of these combine to make us able to measure the stellar density of WASP-4 to extreme precision.

A detailed exploration of what contributes to the statistical precision of ρ_* and an exhaustive search for the best candidate(s) is beyond the scope of this paper, but for the reasons above, WASP-4 is likely among the best suited exoplanet hosts for measuring ρ_* . At any rate, for using ρ_* to measure R_* and T_{eff} , there are diminishing returns beyond a ρ_* precision of $\sim 2\%$ because the systematic floor in M_* begins to dominate.

Because of the way the evolutionary model is implemented with EXOFASTv2, we can only impose error floors in derived quantities like Age, R_* , $[\text{Fe}/\text{H}]$, and T_{eff} , not the grid parameters M_* , $[\text{Fe}/\text{H}]_0$, and EEP. Further, it was unclear to us how the systematic floors from the evolutionary models might combine with the systematic floors from the atmospheric models within EXOFASTv2. We presume that both are limited by our understanding of the underlying stellar astrophysics, and so they should not combine as independent constraints. Instead, the combined MIST+SED models

should still be limited by these same systematic floors: 2% in F_{bol} , 4.2% in R_* , 5% in M_* , 2.4% in T_{eff} , and 0.08 dex in $[\text{Fe}/\text{H}]$.

We began by doing a preliminary fit of only the WASP-4 host star including an SED fit of *Gaia*, 2MASS, and WISE broadband photometry; a MIST stellar evolutionary model ([Dotter 2016](#); [Choi et al. 2016](#); [Paxton et al. 2011, 2013, 2015](#)); priors on $[\text{Fe}/\text{H}] = -0.03 \pm 0.09$ ([Gillon et al. 2009](#)), parallax = 3.797 ± 0.061 mas ([Gaia Collaboration et al. 2018](#)); and an upper limit on the V-band extinction of 0.04278 mag based on galactic dust maps ([Schlegel et al. 1998](#); [Schlafly & Finkbeiner 2011](#)). While a spectroscopic prior was available for T_{eff} , we chose not to use it, as the $\sim 2.4\%$ systematic uncertainty expected is much higher than the uncertainty we expect from our method described in §2.3. For reference, [Wilson et al. \(2008\)](#) found $T_{\text{eff}} = 5500 \pm 150$ K using CORALIE, [Gillon et al. \(2009\)](#) found $T_{\text{eff}} = 5470 \pm 130$ K using IRFM.

We first fit a MIST+SED model with floors in the evolutionary model R_* of 4.2%, T_{eff} of 2.4%, and $[\text{Fe}/\text{H}]$ of 0.08 dex, and SED model floors of 2% in L_* , 2.4% in T_{eff} , and 0.08 dex in $[\text{Fe}/\text{H}]$. However, the combined constraint was lower than our model floors should be trusted. So we inflated the R_* , T_{eff} , and $[\text{Fe}/\text{H}]$ systematic floors by $\sqrt{2}$ as described in §4 and refit. In this way, we were able to impose the desired floors in the MIST+SED fit due to our lack of understanding in the evolutionary and atmospheric stellar models. In the MIST+SED column of table 3, we see that our final constraints are consistent with our desired floors: 2.9% in F_{bol} , 4.1% in R_* , 6.2% in M_* , 2.1% in T_{eff} , and 0.08 dex in $[\text{Fe}/\text{H}]$. The slightly smaller T_{eff} uncertainty follows from equation 8 given the floors in L_* and R_* .

Next, we performed 8 different fits of the WASP-4 system with all combinations of with and without the SED model, the MIST model, and the transit model, including no model constraints, labeled “None,” showing just our prior constraints. Each fit was constrained with the same wide, uniform priors summarized in Table 2, equal to five times the 68% confidence interval of the preliminary MIST+SED fit described above. These are wide enough not to appreciably influence fits that were reasonably well constrained, but narrow enough to allow the fits to mix in the absence of any external constraints, see the impact of our chosen stepping parameters, and ensure that the only thing that changed between fits was the models used to constrain them. In the case where we do not fit the SED, MIST, or transit model, the posteriors are equal to these priors. All fits had systematic error floors imposed, but the two fits that include both MIST and SED further inflate them by square root 2 as described above.

For all fits including transits, we included the 14 discovery RVs from CORALIE ([Wilson et al. 2008](#)), 8 early, complete light curves [Wilson et al. \(2008\)](#); [Gillon et al. \(2009\)](#); [Winn et al. \(2009\)](#) and the flattened, 2-minute SPOC TESS light

Table 2. Priors imposed on all WASP-4b fits

Parameter	Units	Prior
M_* ..	Mass (M_\odot)	$\mathcal{U}[0.694, 1.104]$
R_* ...	Radius (R_\odot)	$\mathcal{U}[0.83, 0.97]$
T_{eff} ..	Effective Temperature (K) .	$\mathcal{U}[5120, 5735]$
[Fe/H]	Metallicity (dex)	$\mathcal{G}[-0.03, 0.09]$
A_V ..	V-band extinction (mag) ..	$\mathcal{U}[0, 0.04278]$
ϖ ...	Parallax (mas)	$\mathcal{G}[3.7965, 0.0608]$
e ...	Eccentricity	0 (fixed)
ω_* ..	Argument of periastron (deg)	90 (fixed)

curves from sectors 2, 28, and 29. The transit data spanned 13 years and 3545 epochs. We disabled the limb darkening table look up from [Claret & Bloemen \(2011\)](#) to avoid introducing any systematic errors ([Patel & Espinoza 2022](#)) and fit the quadratic limb darkening parameters in each band directly. We assumed the orbit was circular.

In figure 10, we show the corner plot of the stellar parameters for the three most relevant fits – the MIST+SED, Transit-only, and MIST+Transit+SED. As expected, we see ρ_* uncertainty is dramatically reduced with the transit, and due to its covariance with R_* and T_{eff} , their uncertainties are also significantly reduced. We also see that the combination of MIST, SED, and the transit is somewhat more complex than our mathematical assumption that the errors are Gaussian and uncorrelated. The slight covariance between M_* and R_* in the MIST+SED fit means that when we add the transit, we also slightly improve the constraint on M_* ($\sim 10\%$).

As can be seen in the last column of Table 3, using MIST, the SED, and the transit model allows us to measure the stellar density to 1.2%. Despite the models using the floors above, we are able to infer M_* to 5.1%, R_* to 1.7%, and T_{eff} to 1.2%, in line with our analytic expectations given such a precise ρ_* . We note that here we do not achieve the 0.9% precision expected from Figure 4 because the uncertainty in the distance is not negligible and we do not reach the floor in F_{bol} , likely because WASP-4 is a relatively faint planet host ($V=12.5$). With the $\sigma_d = 1.6\%$, $\sigma_{F_{\text{bol}}} = 2.7\%$, and $\sigma_{R_*} = 1.7\%$ we achieve, equation 10 predicts a $\sigma_{T_{\text{eff}}} = 1.3\%$, in good agreement with our measurement.

The improvement of the planetary parameters, summarized in Tables 4 and 5, is also significant. However, we must be careful because EXOFASTv2 cannot sever the connection between the transit model and the stellar density. Table 4 shows all the fits that include the transit, and so are direct outputs from EXOFASTv2. Table 5 shows the re-derived planetary parameters using the star-only values in the correspond-

ing column of Table 3 combined with the transit-observables taken from the transit-only fit – thus recreating methods that models the star and planet separately.

These transit-observables span all columns in Table 5 and agree with each other to at least 0.1σ in all fits using a transit in Table 4. Thus, comparing the MIST+Transit+SED column in Table 4 with the MIST+SED column in Table 5 shows the improvement in the planetary parameters that is achievable when we account for realistic systematic floors in the stellar models, we have a strong constraint on stellar density, and we model the star and planet simultaneously.

Most important, the precision in the planet’s radius, density, surface gravity, semi-major axis, and incident flux improve by about a factor of two. The improvement in T_{eq} is equally significant, but it is likely that our statistical uncertainties are dominated by the assumptions that there is no albedo and perfect redistribution. However, the incident flux is an important, fundamental component of the detailed atmospheric modeling necessary to truly understand the equilibrium temperature and habitability more broadly.

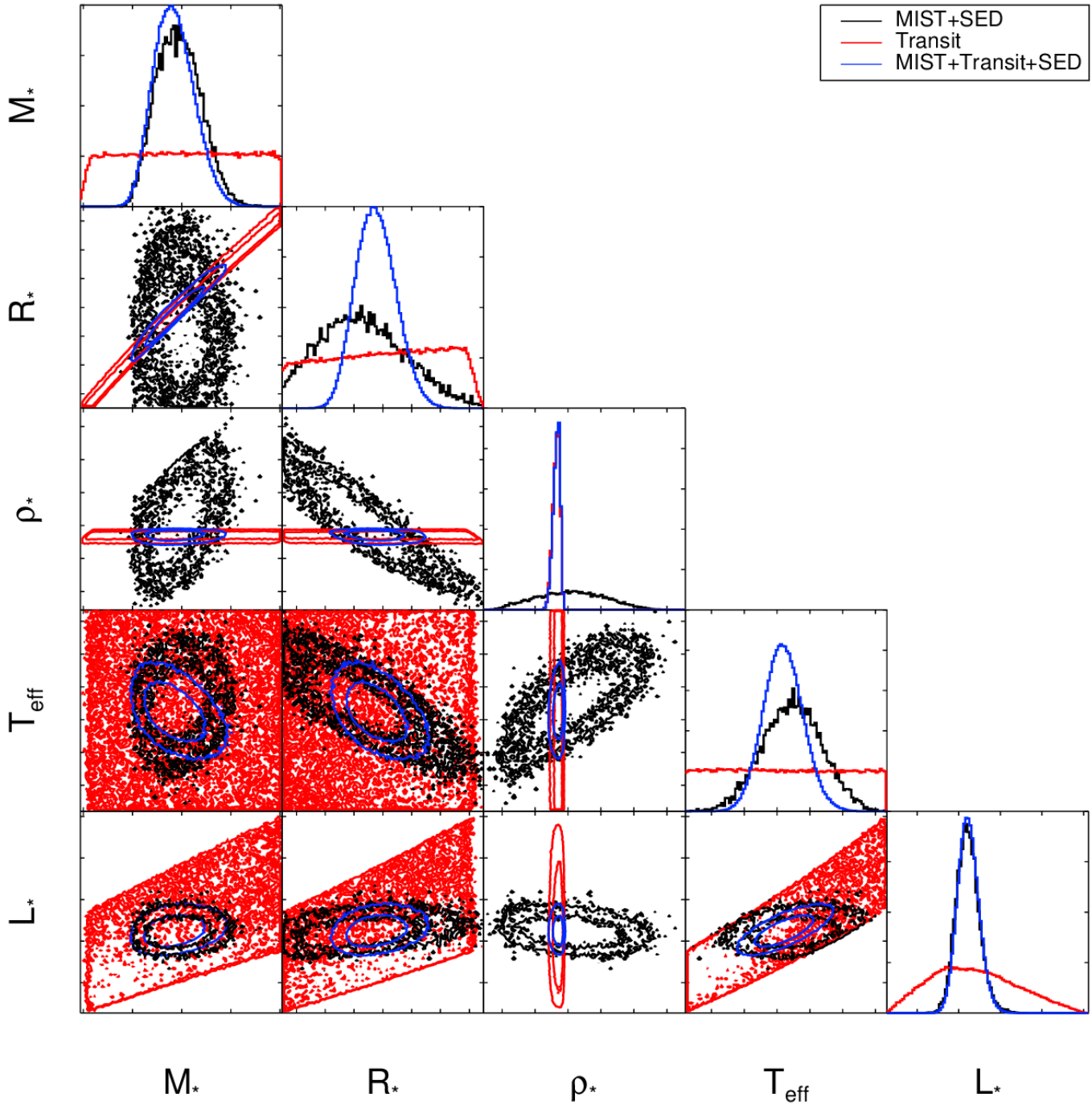


Figure 10. A corner plot of the WASP-4 stellar parameters. The contours show the 68% and 95% confidence intervals for the MIST+SED fit (black), the transit fit (red), and the MIST+Transit+SED fit (blue). From this, we can see just how the addition of the transit constrains the stellar density and significantly improves the precision of R_* and T_{eff} – to well beyond the systematic floors imposed on the SED and MIST evolutionary models.

Table 3. Median values and 68% confidence interval for the WASP-4 host star

Parameter	Units	None	MIST	SED	MIST+SED	Transit	Transit+SED	MIST+Transit	MIST+Transit+SED
M_* ...	Mass (M_\odot) ...	$0.88^{+0.15}_{-0.13}$	$0.882^{+0.055}_{-0.047}$	$0.88^{+0.15}_{-0.13}$	$0.894^{+0.054}_{-0.047}$	0.91 ± 0.14	$0.87^{+0.12}_{-0.10}$	$0.890^{+0.068}_{-0.056}$	$0.888^{+0.049}_{-0.043}$
R_* ...	Radius (R_\odot) ...	0.900 ± 0.047	$0.889^{+0.049}_{-0.040}$	$0.888^{+0.041}_{-0.036}$	$0.888^{+0.039}_{-0.034}$	$0.903^{+0.043}_{-0.048}$	$0.890^{+0.040}_{-0.036}$	$0.898^{+0.023}_{-0.020}$	$0.897^{+0.016}_{-0.015}$
L_* ...	Luminosity (L_\odot) ...	$0.631^{+0.11}_{-0.098}$	$0.63^{+0.12}_{-0.10}$	$0.625^{+0.028}_{-0.026}$	$0.625^{+0.027}_{-0.026}$	$0.632^{+0.12}_{-0.098}$	$0.624^{+0.026}_{-0.025}$	0.65 ± 0.11	$0.624^{+0.027}_{-0.025}$
ρ_* ...	Density (cgs) ...	$1.70^{+0.38}_{-0.31}$	$1.77^{+0.23}_{-0.24}$	$1.75^{+0.36}_{-0.30}$	$1.80^{+0.25}_{-0.23}$	$1.737^{+0.019}_{-0.024}$	$1.738^{+0.019}_{-0.024}$	$1.739^{+0.019}_{-0.024}$	$1.739^{+0.018}_{-0.024}$
$\log g$..	Surface gravity (cgs)	4.473 ± 0.074	$4.486^{+0.037}_{-0.041}$	4.482 ± 0.073	4.492 ± 0.043	$4.484^{+0.020}_{-0.024}$	$4.478^{+0.019}_{-0.018}$	$4.4816^{+0.011}_{-0.0099}$	$4.4813^{+0.0085}_{-0.0081}$
T_{eff} ...	Effective Temp (K)	5430 ± 210	5450^{+170}_{-190}	5440^{+110}_{-120}	5440 ± 110	5420 ± 210	5440 ± 110	5470^{+170}_{-200}	5416^{+67}_{-65}
$[\text{Fe}/\text{H}]$.	Metallicity (dex) ..	-0.030 ± 0.088	$-0.022^{+0.089}_{-0.090}$	$0.011^{+0.086}_{-0.083}$	$0.014^{+0.083}_{-0.082}$	-0.030 ± 0.090	$0.013^{+0.084}_{-0.079}$	$-0.020^{+0.089}_{-0.088}$	$0.016^{+0.082}_{-0.079}$
$R_{*,\text{SED}}$.	Radius ¹ (R_\odot) ...	-	-	$0.883^{+0.017}_{-0.016}$	$0.882^{+0.017}_{-0.016}$	-	0.883 ± 0.016	-	$0.882^{+0.016}_{-0.015}$
F_{bol} ...	Bol Flux $\times 10^{10}$ (cgs)	-	-	$2.866^{+0.089}_{-0.077}$	$2.867^{+0.088}_{-0.076}$	-	$2.865^{+0.080}_{-0.073}$	-	$2.864^{+0.082}_{-0.074}$
$T_{\text{eff,SED}}$.	Effective Temp ¹ (K)	-	-	5461^{+34}_{-31}	5463^{+33}_{-31}	-	5460^{+30}_{-29}	-	5460^{+30}_{-29}
$[\text{Fe}/\text{H}]_{\text{SED}}$.	Metallicity ¹ (dex) .	-	-	$0.040^{+0.11}_{-0.094}$	$0.043^{+0.11}_{-0.094}$	-	$0.044^{+0.11}_{-0.090}$	-	$0.044^{+0.11}_{-0.090}$
A_V ...	V-band ext (mag) .	-	-	$0.023^{+0.014}_{-0.015}$	$0.023^{+0.014}_{-0.016}$	-	$0.023^{+0.014}_{-0.015}$	-	$0.022^{+0.014}_{-0.015}$
σ_{SED} ...	SED phot err scaling	-	-	$1.02^{+0.42}_{-0.24}$	$1.00^{+0.40}_{-0.24}$	-	$0.97^{+0.33}_{-0.21}$	-	$0.97^{+0.34}_{-0.21}$
ϖ ...	Parallax (mas) ...	-	-	3.790 ± 0.062	$3.789^{+0.061}_{-0.062}$	-	3.788 ± 0.060	-	$3.789^{+0.059}_{-0.060}$
d ...	Distance (pc) ...	-	-	$263.9^{+4.4}_{-4.2}$	$263.9^{+4.4}_{-4.2}$	-	$264.0^{+4.2}_{-4.1}$	-	$263.9^{+4.2}_{-4.1}$
$[\text{Fe}/\text{H}]_0$.	Initial Metallicity ² .	-	0.00 ± 0.10	-	0.03 ± 0.10	-	-	0.01 ± 0.10	$0.034^{+0.10}_{-0.099}$
Age ...	Age (Gyr) ...	-	$7.0^{+4.4}_{-3.6}$	-	$6.5^{+4.7}_{-4.1}$	-	-	$6.9^{+4.3}_{-4.0}$	7.1 ± 3.9
EEP ..	Equal Evol Phase ³ .	-	352^{+36}_{-18}	-	350^{+37}_{-27}	-	-	354^{+30}_{-21}	354^{+33}_{-22}

See Table 3 in Eastman et al. (2019) for a detailed description of all parameters

¹ This value ignores the systematic error and is for reference only² The metallicity of the star at birth³ Corresponds to static points in a star's evolutionary history. See §2 in Dotter (2016).

Table 4. Median values and 68% confidence interval for the WASP-4 host star

Parameter	Units	Transit	Transit+SED	MIST+Transit	MIST+Transit+SED
P ...	Period (days) ...	1.338231512 ± 0.000000019	1.338231512 ± 0.000000019	1.338231513 ± 0.000000019	1.338231512 ± 0.000000019
R_p ...	Radius (R_J) ...	1.348 ^{+0.064} _{-0.071}	1.330 ^{+0.059} _{-0.054}	1.341 ^{+0.033} _{-0.029}	1.339 ^{+0.025} _{-0.023}
M_p ...	Mass (M_J) ...	1.22 ± 0.13	1.19 ^{+0.12} _{-0.11}	1.210 ^{+0.085} _{-0.079}	1.208 ^{+0.075} _{-0.073}
T_C ...	Time of conjunction ⁴ (BJD _{TDB}) ...	2454697.797524 ± 0.000024	2454697.797525 ± 0.000024	2454697.797524 ^{+0.000024} _{-0.000023}	2454697.797524 ^{+0.000024} _{-0.000023}
T_T ...	Time of min proj sep ⁵ (BJD _{TDB}) ...	2454697.797524 ± 0.000024	2454697.797525 ± 0.000024	2454697.797524 ^{+0.000024} _{-0.000023}	2454697.797524 ^{+0.000024} _{-0.000023}
T_0 ...	Optimal conj Time ⁶ (BJD _{TDB}) ...	2455334.795723 ± 0.000022	2455349.516272 ± 0.000022	2455326.766335 ± 0.000022	2455328.104567 ± 0.000022
a ...	Semi-major axis (AU) ...	0.0230 ^{+0.0011} _{-0.0012}	0.02268 ^{+0.0010} _{-0.00092}	0.02287 ^{+0.00058} _{-0.00050}	0.02284 ^{+0.00043} _{-0.00040}
i ...	Inclination (Degrees) ...	88.86 ^{+0.65} _{-0.51}	88.88 ^{+0.66} _{-0.56}	88.90 ^{+0.65} _{-0.51}	88.90 ^{+0.65} _{-0.50}
T_{eq} ...	Equilibrium temperature ⁷ (K) ...	1638 ⁺⁶⁴ ₋₆₂	1642 ⁺³³ ₋₃₄	1653 ⁺⁵³ ₋₅₀	1636 ⁺²¹ ₋₂₀
τ_{circ} ...	Tidal circ timescale (Gyr) ...	0.00277 ^{+0.00021} _{-0.00020}	0.00280 ± 0.00021	0.00278 ^{+0.00018} _{-0.00019}	0.00278 ± 0.00018
K ...	RV semi-amplitude (m/s) ...	240 ± 12	240 ± 12	240 ± 12	240 ± 12
R_p/R_* ...	Radius of planet in stellar radii ...	0.15349 ^{+0.00047} _{-0.00040}	0.15348 ^{+0.00046} _{-0.00039}	0.15347 ^{+0.00046} _{-0.00039}	0.15347 ^{+0.00046} _{-0.00039}
a/R_* ...	Semi-major axis in stellar radii ...	5.481 ^{+0.020} _{-0.026}	5.482 ^{+0.020} _{-0.026}	5.483 ^{+0.019} _{-0.026}	5.483 ^{+0.019} _{-0.025}
δ ...	$(R_p/R_*)^2$...	0.02356 ^{+0.00014} _{-0.00012}	0.02355 ^{+0.00014} _{-0.00012}	0.02355 ^{+0.00014} _{-0.00012}	0.02355 ^{+0.00014} _{-0.00012}
δ_R ...	Transit depth in R (fraction) ...	0.03043 ^{+0.00087} _{-0.00082}	0.03042 ^{+0.00086} _{-0.00082}	0.03043 ^{+0.00085} _{-0.00081}	0.03043 ^{+0.00086} _{-0.00081}
$\delta_{z'}$...	Transit depth in z' (fraction) ...	0.02782 ^{+0.00049} _{-0.00047}	0.02781 ^{+0.00049} _{-0.00046}	0.02782 ^{+0.00049} _{-0.00046}	0.02781 ^{+0.00048} _{-0.00046}
δ_{TESS} ...	Transit depth in TESS (fraction) ...	0.02869 ^{+0.00076} _{-0.00072}	0.02867 ^{+0.00076} _{-0.00070}	0.02868 ^{+0.00075} _{-0.00071}	0.02866 ^{+0.00076} _{-0.00070}
τ ...	Ingress/egress transit duration (days) ...	0.01221 ^{+0.00017} _{-0.00013}	0.01220 ^{+0.00017} _{-0.00013}	0.01220 ^{+0.00017} _{-0.00012}	0.01219 ^{+0.00017} _{-0.00012}
T_{14} ...	Total transit duration (days) ...	0.08992 ± 0.00014	0.08992 ± 0.00014	0.08992 ± 0.00014	0.08992 ± 0.00014
T_{FWHM} ...	FWHM transit duration (days) ...	0.07770 ^{+0.00017} _{-0.00018}	0.07770 ^{+0.00017} _{-0.00018}	0.07770 ^{+0.00017} _{-0.00018}	0.07770 ^{+0.00017} _{-0.00018}
b ...	Transit impact parameter ...	0.109 ^{+0.048} _{-0.062}	0.107 ^{+0.048} _{-0.063}	0.105 ^{+0.048} _{-0.062}	0.105 ^{+0.048} _{-0.062}
ρ_p ...	Density (cgs) ...	0.619 ^{+0.045} _{-0.042}	0.626 ± 0.041	0.622 ± 0.036	0.623 ± 0.034
$\log g_p$...	Surface gravity (cgs) ...	3.222 ^{+0.021} _{-0.023}	3.222 ^{+0.021} _{-0.023}	3.222 ^{+0.021} _{-0.023}	3.222 ^{+0.021} _{-0.023}
$\langle F \rangle$...	Incident Flux ($10^9 \text{ erg s}^{-1} \text{ cm}^{-2}$) ...	1.64 ^{+0.27} _{-0.24}	1.65 ^{+0.14} _{-0.13}	1.69 ± 0.23	1.626 ^{+0.084} _{-0.078}
T_S ...	Time of eclipse (BJD _{TDB}) ...	2454698.466639 ± 0.000024	2454698.466641 ± 0.000024	2454698.466640 ^{+0.000024} _{-0.000023}	2454697.128408 ^{+0.000024} _{-0.000023}
$M_p \sin i$...	Minimum mass (M_J) ...	1.22 ± 0.13	1.19 ^{+0.12} _{-0.11}	1.210 ^{+0.085} _{-0.079}	1.208 ^{+0.075} _{-0.073}
u_1 ...	R linear limb-darkening coeff ...	0.460 ± 0.042	0.460 ± 0.041	0.460 ± 0.041	0.460 ± 0.041
u_2 ...	R quadratic limb-darkening coeff ...	0.151 ^{+0.075} _{-0.076}	0.152 ^{+0.074} _{-0.075}	0.152 ^{+0.074} _{-0.075}	0.152 ± 0.075
u_1' ...	z' linear limb-darkening coeff ...	0.313 ± 0.025	0.312 ^{+0.025} _{-0.024}	0.313 ^{+0.025} _{-0.024}	0.312 ^{+0.025} _{-0.024}
u_2' ...	z' quadratic limb-darkening coeff ...	0.218 ^{+0.056} _{-0.058}	0.220 ^{+0.055} _{-0.057}	0.219 ^{+0.055} _{-0.057}	0.219 ^{+0.055} _{-0.056}
u_1'' ...	TESS linear limb-darkening coeff ...	0.365 ± 0.041	0.364 ^{+0.041} _{-0.040}	0.364 ± 0.040	0.364 ^{+0.040} _{-0.039}
u_2'' ...	TESS quadratic limb-darkening coeff ...	0.139 ^{+0.075} _{-0.076}	0.141 ^{+0.073} _{-0.075}	0.140 ± 0.074	0.141 ^{+0.073} _{-0.075}

See Table 3 in Eastman et al. (2019) for a detailed description of all parameters

⁴Time of conjunction is commonly reported as the "transit time"⁵Time of minimum projected separation is a more correct "transit time"⁶Optimal time of conjunction minimizes the covariance between T_C and Period⁷ Assumes no albedo and perfect redistribution

Table 5. Median values and 68% confidence interval for WASP-4b planet fits, separating the transit and stellar models. Values that span all columns are taken from the transit-only fit.

Parameter	Units	None	MIST	SED	MIST+SED
P ...	Period (days)		1.338231512 ± 0.000000019		
R_P ...	Radius (R_J)	1.345 ± 0.070	1.328 ^{+0.073} _{-0.060}	1.328 ^{+0.062} _{-0.053}	1.327 ^{+0.058} _{-0.051}
M_P ..	Mass (M_J)	1.19 ^{+0.14} _{-0.12}	1.203 ^{+0.078} _{-0.074}	1.20 ^{+0.14} _{-0.13}	1.213 ^{+0.078} _{-0.076}
T_C ...	Time of conjunction ⁴ (BJD _{TDB}) ..		2454697.797524 ± 0.000024		
T_T ...	Time of min proj sep ⁵ (BJD _{TDB}) ..		2454697.797524 ± 0.000024		
T_0 ...	Optimal conj Time ⁶ (BJD _{TDB}) ...		2455334.795723 ± 0.000022		
a ...	Semi-major axis (AU)	0.0229 ± 0.0012	0.0226 ^{+0.0013} _{-0.0010}	0.02264 ^{+0.0011} _{-0.00091}	0.02263 ^{+0.00099} _{-0.00087}
i ...	Inclination (Degrees)		88.86 ^{+0.65} _{-0.51}		
T_{eq} ..	Equilibrium temperature ⁷ (K) ...	1639 ± 62	1646 ⁺⁵³ ₋₅₆	1644 ⁺³³ ₋₃₅	1644 ⁺³³ ₋₃₄
τ_{circ} ..	Tidal circ timescale (Gyr)	0.00282 ^{+0.00046} _{-0.00040}	0.00276 ^{+0.00027} _{-0.00024}	0.00278 ^{+0.00045} _{-0.00038}	0.00273 ^{+0.00028} _{-0.00026}
K ...	RV semi-amplitude (m/s)		240 ± 12		
R_P/R_* ..	Radius of planet in stellar radii ...		0.15349 ^{+0.00047} _{-0.00040}		
a/R_* ..	Semi-major axis in stellar radii ..		5.481 ^{+0.020} _{-0.026}		
δ ...	$(R_P/R_*)^2$		0.02356 ^{+0.00014} _{-0.00012}		
δ_R ...	Transit depth in R (fraction)		0.03043 ^{+0.00087} _{-0.00082}		
$\delta_{z'}$..	Transit depth in z' (fraction)		0.02782 ^{+0.00049} _{-0.00047}		
δ_{TESS} ..	Transit depth in TESS (fraction) ..		0.02869 ^{+0.00076} _{-0.00072}		
τ ...	Ingress/egress transit duration (days)		0.01221 ^{+0.00017} _{-0.00013}		
T_{14} ...	Total transit duration (days)		0.08992 ± 0.00014		
T_{FWHM}	FWHM transit duration (days) ...		0.07770 ^{+0.00017} _{-0.00018}		
b ...	Transit impact parameter		0.109 ^{+0.048} _{-0.062}		
ρ_P ...	Density (cgs)	0.610 ^{+0.12} _{-0.099}	0.635 ^{+0.092} _{-0.090}	0.632 ^{+0.11} _{-0.096}	0.642 ^{+0.092} _{-0.085}
$\log g_P$..	Surface gravity (cgs)	3.215 ^{+0.061} _{-0.062}	3.227 ^{+0.042} _{-0.046}	3.224 ± 0.058	3.231 ^{+0.044} _{-0.046}
$\langle F \rangle$..	Incident Flux (10^9 erg s ⁻¹ cm ⁻²) ..	1.64 ^{+0.26} _{-0.24}	1.67 ± 0.22	1.66 ± 0.14	1.66 ^{+0.14} _{-0.13}
T_S ...	Time of eclipse (BJD _{TDB})		2454698.466639 ± 0.000024		
$M_P \sin i$	Minimum mass (M_J)	1.19 ^{+0.14} _{-0.12}	1.203 ^{+0.078} _{-0.074}	1.20 ^{+0.14} _{-0.13}	1.213 ^{+0.078} _{-0.076}
u_1 ...	R linear limb-darkening coeff ...		0.460 ± 0.042		
u_2 ...	R quadratic limb-darkening coeff .		0.151 ^{+0.075} _{-0.076}		
u_1 ...	z' linear limb-darkening coeff ...		0.313 ± 0.025		
u_2 ...	z' quadratic limb-darkening coeff .		0.218 ^{+0.056} _{-0.058}		
u_1 ...	TESS linear limb-darkening coeff .		0.365 ± 0.041		
u_2 ...	TESS quadratic limb-darkening coeff		0.139 ^{+0.075} _{-0.076}		

See Table 3 in Eastman et al. (2019) for a detailed description of all parameters

⁴Time of conjunction is commonly reported as the "transit time"⁵Time of minimum projected separation is a more correct "transit time"⁶Optimal time of conjunction minimizes the covariance between T_C and Period⁷Assumes no albedo and perfect redistribution

6. DISCUSSION

Among the set of 1151 default (DEFAULT_FLAG=1) transiting planets (TRAN_FLAG=1) in the exoplanet archive where the stellar density and its uncertainty is populated, 56 have host stars with a fractional ρ_* uncertainty less than 2%. It grows to 426 systems if we use a threshold of 9% (where we can beat the systematic floor in the SED/MIST-derived $\log g_*$), 549 systems if we use a threshold of 11.5% (where we can beat the systematic floor in the SED/MIST-derived R_*), and 601 systems if we use a threshold of 13% (where we can beat the systematic floor in the spectroscopic T_{eff}).

These are likely a significant undercount of the number of systems suitable to such precision given the heterogeneity of the sample, the relative rarity of simultaneous modeling of the star and planet, and the fact that only 30% of the default set of transiting planets have densities populated. It is possible that some of these densities are optimistically derived from evolutionary models while ignoring systematic errors rather than a transit light curve. However, only 6% of non-transiting planets have quoted stellar densities compared to 30% of transiting planets, implying the transit was used for most when available.

Regardless, this technique could likely be applied to a significant fraction of transiting planet hosts to improve the stellar and planetary parameters. Even non-transiting planet hosts are likely to see improved $\log g_*$ precision, as described in §2.5. While a precision similar to what we achieve here is commonly reported in the literature, few have accounted for the systematic uncertainties in the stellar parameters shown by Tayar et al. (2022), and so may be too optimistic.

The results shown here emphasize just how important it is to model the star along with the planet to improve the precision of both. It is possible that a large sample of well-measured transit light curves may even help inform stellar models. This method is competitive with gold standard measurements like asteroseismology or eclipsing binary stars, but broadens the pool of applicable stars dramatically. This, in turn, could give us a precise probe into stellar parameters that enable us to test and refine the evolutionary models. Be-

cause our derived parameters are still limited by systematics in the stellar models, further improvement in stellar models would yield additional refinement with currently known stellar densities. It may even be fruitful to explore how best to take advantage of the precise stellar density and bolometric flux constraints when constructing the evolutionary models themselves, as these are directly and precisely measured for a much larger sample of stars than are typically used to anchor stellar models.

Work by J.D.E. was funded NASA ADAP 80NSSC19K1014. Computations in this paper were run on the Canon cluster supported by the FAS Division of Science, Research Computing Group at Harvard University.

This research has made use of the NASA Exoplanet Archive, which is operated by the California Institute of Technology, under contract with the National Aeronautics and Space Administration under the Exoplanet Exploration Program.

This work has made use of data from the European Space Agency (ESA) mission *Gaia* (<https://www.cosmos.esa.int/gaia>), processed by the *Gaia* Data Processing and Analysis Consortium (DPAC, <https://www.cosmos.esa.int/web/gaia/dpac/consortium>). Funding for the DPAC has been provided by national institutions, in particular the institutions participating in the *Gaia* Multilateral Agreement.

This publication makes use of data products from the Two Micron All Sky Survey, which is a joint project of the University of Massachusetts and the Infrared Processing and Analysis Center/California Institute of Technology, funded by the National Aeronautics and Space Administration and the National Science Foundation.

This publication makes use of data products from the Wide-field Infrared Survey Explorer, which is a joint project of the University of California, Los Angeles, and the Jet Propulsion Laboratory/California Institute of Technology, funded by the National Aeronautics and Space Administration.

Facilities: Exoplanet Archive, Gaia, FLWO:2MASS, CTIO:2MASS, WISE

REFERENCES

- Adams, F. C., & Laughlin, G. 2006, *ApJ*, 649, 1004
 Beatty, T. G., Stevens, D. J., Collins, K. A., et al. 2017, *AJ*, 154, 25
 Choi, J., Dotter, A., Conroy, C., et al. 2016, *ApJ*, 823, 102
 Claret, A., & Bloemen, S. 2011, *A&A*, 529, A75
 Dotter, A. 2016, *ApJS*, 222, 8
 Eastman, J., Gaudi, B. S., & Agol, E. 2013, *PASP*, 125, 83
 Eastman, J. D., Rodriguez, J. E., Agol, E., et al. 2019, arXiv e-prints, arXiv:1907.09480
 Gaia Collaboration, Brown, A. G. A., Vallenari, A., et al. 2016, *A&A*, 595, A2
 —. 2018, *A&A*, 616, A1
 Gillon, M., Smalley, B., Hebb, L., et al. 2009, *A&A*, 496, 259
 Lindegren, L., Hernández, J., Bombrun, A., et al. 2018, *A&A*, 616, A2
 Lindegren, L., Bastian, U., Biermann, M., et al. 2021, *A&A*, 649, A4

- Mandel, K., & Agol, E. 2002, *ApJL*, 580, L171
- Patel, J. A., & Espinoza, N. 2022, *AJ*, 163, 228
- Paxton, B., Bildsten, L., Dotter, A., et al. 2011, *ApJS*, 192, 3
- Paxton, B., Cantiello, M., Arras, P., et al. 2013, *ApJS*, 208, 4
- Paxton, B., Marchant, P., Schwab, J., et al. 2015, *ApJS*, 220, 15
- Schlafly, E. F., & Finkbeiner, D. P. 2011, *ApJ*, 737, 103
- Schlegel, D. J., Finkbeiner, D. P., & Davis, M. 1998, *ApJ*, 500, 525
- Seager, S., & Mallén-Ornelas, G. 2003, in *Astronomical Society of the Pacific Conference Series*, Vol. 294, *Scientific Frontiers in Research on Extrasolar Planets*, ed. D. Deming & S. Seager, 419–422
- Skrutskie, M. F., Cutri, R. M., Stiening, R., et al. 2006, *AJ*, 131, 1163
- Stassun, K. G., & Torres, G. 2018, *ApJ*, 862, 61
- Stevens, D. J., Gaudi, B. S., & Stassun, K. G. 2018, *The Astrophysical Journal*, 862, 53
- Tayar, J., Claytor, Z. R., Huber, D., & van Saders, J. 2022, *ApJ*, 927, 31
- Torres, G., Fischer, D. A., Sozzetti, A., et al. 2012, *ApJ*, 757, 161
- Wilson, D. M., Gillon, M., Hellier, C., et al. 2008, *ApJL*, 675, L113
- Winn, J. N. 2010, arXiv e-prints, arXiv:1001.2010
- Winn, J. N., Holman, M. J., Carter, J. A., et al. 2009, *AJ*, 137, 3826
- Winn, J. N., Holman, M. J., Torres, G., et al. 2008, *ApJ*, 683, 1076
- Wright, E. L., Eisenhardt, P. R. M., Mainzer, A. K., et al. 2010, *AJ*, 140, 1868
- Zinn, J. C., Pinsonneault, M. H., Huber, D., & Stello, D. 2019, *ApJ*, 878, 136